J Solid State Electrochem (2012) 16:633–648
DOI 10.1007/s10008-011-1403-y

ORIGINAL PAPER

# Corrosion behavior in artificial seawater of thermal-sprayed WC-CoCr coatings on mild steel by electrochemical impedance spectroscopy

**S. Brioua · K. Belmokre · V. Debout · P. Jacquot · E. Conforto · S. Touzain · J. Creus**

Received: 20 December 2010 / Revised: 22 March 2011 / Accepted: 11 April 2011 / Published online: 4 May 2011


**Abstract** The corrosion behavior in artificial seawater of different as-sprayed ceramic-metallic (cermet) coatings applied on low-alloy steel was studied. Five conditions, associated to modifications of the composition of the powder or deposition parameters were evaluated. The degradation mechanisms were studied during extended immersion tests using conventional electrochemical measurement and electrochemical impedance spectroscopy. The extended immersion tests reveal that these as-thermal-sprayed coatings present a cathodic behavior compared with steel. During the first hours of immersion, the electrolyte infiltrates the defects of the coatings, which then result to the local degradation of the substrate accelerated by the galvanic coupling with the cermet coating. Optical observations and Raman analyses reveal the formation of calcium carbonates like aragonite on the cermet surface, very close to the appearance of local anodic sites. The cross-sectioned views reveal the infiltration of the corrosive solution, and the depth penetration of the degradation of steel substrate probably due to the acidification of the anodic sites.

**Keywords** WC-CoCr coatings · Thermal spray · Corrosion · EIS · Seawater

S. Brioua · K. Belmokre
LCTS, Université de Skikda,
Route Elhadeik, BP 26,
21000 Skikda, Algeria

V. Debout
Bodycote Surface Technology,
10 Rue Gustave Eiffel,
87240 Ambazac, France

P. Jacquot
Bodycote,
Rue Ampère,
69330 Pusignan, France

E. Conforto
CCA FR-EDD, Université de la Rochelle,
Avenue Michel Crépeau,
17042 La Rochelle, France

S. Touzain · J. Creus (✉)
LEMMA, Université de la Rochelle,
Avenue Michel Crépeau,
17042 La Rochelle, France
e-mail: jcreus@univ-lr.fr

## Introduction

Ceramic-metallic (cermet) coatings are useful when high surface hardness and resistance to wear are required. The hard WC particles in the coating provide hardness and wear resistance while the metal binder (CoCr, NiCr, Ni, Co, etc.) gives the necessary coating toughness [1–3]. High-velocity oxy-fuel (HVOF) thermal sprayings have been designed to retain a larger fraction of WC in the coating. In this method, the hypersonic velocity of the flame shortens the time of interaction between the powder and the flame, and in conjunction with the relatively low temperature in the latter, limits WC decomposition [4].

WC-based hardmetals are usually applied in neutral and near-neutral aqueous working environments. The corrosion process of cermet-coated metallic substrates is a very complex phenomenon. The properties affecting the corrosion performance of coating on a service are the as-spraying coating, the binder material, and the deposition parameters [5]. Several works have underlined the importance of spray parameters and the powder chemical composition on corrosion behavior of HVOF coatings [6–9].

Different studies have been made in order to evaluate the electrochemical behavior of the carbide particle WC and the metallic matrix, respectively. These studies are mainly performed in acidic HCl or $H_2SO_4$ solutions, and it was reported that tungsten carbide particles were nobler than the metallic matrix. A uniform dissolution of the cobalt-based matrix was reported [10–12]. Effectively, in acidic and near-neutral solutions, cobalt suffers from a uniform dissolution and no passivation was observed [11]. Anyway, electrochemical behaviors in near-neutral solutions of thermal-sprayed WC-Co-based coatings reported in literature were not so concordant. Perry et al. [13] had observed that during the anodic polarization of WC-$_{10}Co_4Cr$ in synthetic seawater, removals of carbide particles that suggest an initiation of corrosion at the carbide/metal interface. As the porosity rate of HVOF coatings is very low, less than 1%, it was assumed that interconnected porosity was no longer the main issue in the corrosion behavior of a coating/substrate system. Corrosion process has been shown to be concentrated at the metallic/ceramic interfaces. So, micro-galvanic cells occur between WC carbide particles and the metallic matrix that lead to selective dissolution of the metallic binder [13, 14]. Such observations were also reported for cermet composite coatings deposited onto low-alloy steels [8, 15–17] or aluminum [3, 18] and exposed in saline solution. The main degradation was assigned to the metallic matrix dissolution, and the carbide particles remain unchanged.

However, non-concordant results were presented in the literature concerning the corrosion behavior of such thermal-sprayed composite coatings. Effectively, some studies have reported the observations during extended immersion tests in aggressive solution of corrosion products associated to the substrate degradation [19]. Open-circuit potential evolutions of the coated samples were reported to be quite similar to that of the substrate, indicating behavior where electrolyte easily reaches the base substrate through open defects [2, 9, 20–22]. So, according to these studies, as-sprayed WC-Co-based coatings lead to an ennoblement of the corrosion potential, compared with the substrate. Indeed, corrosion potential of WC particles and pure cobalt were respectively reported to be around +0.19 V/SCE and −0.32 V/SCE [8]. As-sprayed WC-Co-based coatings are nobler than the substrates, and effectively degradation can be localized at the open defects where electrolyte can easily infiltrates until the substrate/coating interface. In this case, galvanic corrosion between coating and substrate may occur accelerating the local dissolution of the substrate [23–26]. Amplification of the localized degradation of the substrate by galvanic corrosion was not described in literature. Galvanic corrosion was reported to occur between the WC particles and the metallic binder, leading to an increase of the surface roughness and the formation of porous corrosion products of cobalt [15]. The objective of this study is to clarify the degradation mechanism of WC-CoCr-coated steel in saline solution. Application development of these tribological-resistant coatings in marine environment needs to thoroughly investigate the degradation of the coated samples and to evaluate the evolution of industrial deposition parameters on the property modifications.

Corrosion behavior using electrochemical impedance spectroscopy (EIS) of as-sprayed WC-CoCr coatings of approximately 250 μm in thickness, deposited onto low-alloy steel by HVOF thermal spraying at different deposition parameters was investigated in artificial seawater. Examination of the corroded samples, completed with analyze techniques would allow to define the mechanism implied in the degradation of the coated samples.

## Experimental

### Samples preparation

WC-CoCr cermets were deposited on a commercial low-alloy steel substrate (35CrMo4 or AISI 4135) by HVOF thermal-spray technique at different deposition parameters using two compositions of powders. Two commercial powders A and B are used in this study; the nominal compositions reported by suppliers are reported in Table 1. Coatings were deposited using HVOF thermal-spray technique at Bodycote in a closed chamber with controlled temperature and projection kinematic. The speed reached by the particles is higher than 700 m/s with a flame temperature around 2,600 °C. Particles passing through the flame are then projected on the rotating substrate surface with the projection gun being animated by a translatory movement. Table 2 summarizes the deposition parameters used during this study. “Standard” deposition corresponds to the conventional optimized parameters used for the industrial deposition of WC-CoCr coatings and these parameters cannot be detailed. The other configurations

**Table 1** Characteristics of the as-received commercial powders

| Powder | Chemical composition (wt.%) | Particle sizes |
|---|---|---|
| A | W, 81.08; C, 5.35; Co, 9.68; Cr, 3.8; Fe, 0.09 | 10~38 μm |
| B | W, 77.7–80.1; C, 5.1–5.8; Co, 8.5–9.5; Cr, 4.5–5.5; Ni, 0.8–1.2; Fe, 0.3 | 15~45 μm |

**Table 2** Deposition parameters of HVOF as-sprayed WC-CoCr coatings

| Ref | Powder | Flame temperature | Powder feed rate | Gun transverse velocity |
|---|---|---|---|---|
| Coating 1 | A | Standard | Standard | Standard |
| Coating 2 | A | Standard | Standard | Reduced |
| Coating 3 | A | Reduced | Standard | Standard |
| Coating 4 | A | Standard | Reduced | Standard |
| Coating 5 | B | Standard | Standard | Standard |

correspond to modification of one parameter compared with the standard condition, for example a reduction of the translatory movement, lowering the flame temperature by modifying the ratio of combustive/fuel, a reduction of the powder flow. So, evolution of the deposition parameters will be discussed in terms of the morphological, microstructural, and corrosion properties of these coatings.

The coatings are made from powders containing small particles of tungsten carbide embedded in a metallic phase, the binder, consisting of Co, Cr, or Ni. The thickness range of as-sprayed coatings was 240–300 μm. The roughness is $R_a$ of 4–5 μm.

### Characterization

The crystalline structures of the coatings was investigated by X-ray diffraction operating with Cu $K_\alpha$ ($\lambda$=0.154056 nm) radiation. The analyzed range of the diffraction angle 2θ° was between 25° and 90°. Samples were observed by an optical LEICA DM6000M microscope in dark field or polarized light and a scanning electron microscope (SEM). Energy dispersive X-ray spectrometer (EDS) was used to characterize powders and coatings with an accelerating voltage of 20 kV.

μ-Raman spectrophotometry was used to characterize the nature of the corrosion products appearing during the aging of coated samples. Raman spectra were recorded with a Jobin Yvon LabRam HR spectrometer using an incident beam of 632.82 nm emitted by an argon laser. Laser power was kept constant around 0.7 mW, and detection was achieved with a Peltier-based cooled charge coupled device detector. Acquisition and basic treatment of spectra were performed with LabSpec software (Jobin Yvon–Horiba). Fourier transform infrared-attenuated total reflectance (FTIR-ATR) measurements were performed with a ThermoNicolet FTIR Nexus spectrometer, and the micro-ATR crystal was a diamond crystal. Spectra were acquired in the range of wavenumber from 500 to 4,000 $cm^{-1}$ using the Omnic software.

**Table 3** Simplified artificial seawater composition according to standard (ASTM D-1141)

| Salts | Concentration (mol $L^{-1}$) | Concentration (g $L^{-1}$) |
|---|---|---|
| NaCl | 0.42 | 24.5448 |
| $Na_2SO_4$ | 0.0288 | 4.0907 |
| $MgCl_2{\cdot}6H_2O$ | 0.0546 | 11.1007 |
| $CaCl_2{\cdot}2H_2O$ | 0.0105 | 1.5437 |
| KCl | 0.00932 | 0.6948 |
| $NaHCO_3$ | 0.002792 | 0.2345 |

### Electrochemical corrosion measurements

Electrochemical impedance spectroscopy was performed at the open-circuit potential using a potentiostat Autolab Pgstat 302 N in a frequency range of $10^5$–$10^{-2}$ Hz with ten points par decade using an amplitude perturbation of 10 mV peak to peak. The experiments were realized during 48 h of immersion in artificial seawater. A three-electrode electrochemical cell was used with a platinum grid counter electrode and a saturated calomel electrode as the reference. The exposed surface area to the corrosive medium was fixed at 2.25 $cm^2$ using an inert resin. All the electrochemical tests were performed in simplified artificial seawater prepared according to standard ASTM D-1141 whose composition is reported in Table 3. pH was adjusted by addition of NaOH 0.1 mol $L^{-1}$ solution at a value of 8.2, and the corrosion tests were conducted in an environment that is naturally ventilated, agitated, and at room temperature. Reproducibility of the electrochemical tests was ensured during this study.

## Results and discussion

### Characterization of spray powders and coatings

Figure 1 shows the morphologies of the particles used for the coating deposition. Both powders are composed of spherical and agglomerated particles. A statistical approach was developed to measure the size distribution of the agglomerated particles characteristics of powders A and B. Different SEM pictures (between 10 and 20) presenting several particles were obtained, at the same magnification, in order to measure a size distribution that was representative from the characterized powder. Powder A had a grain size ranging from 10 to 38 μm with an average grain size of

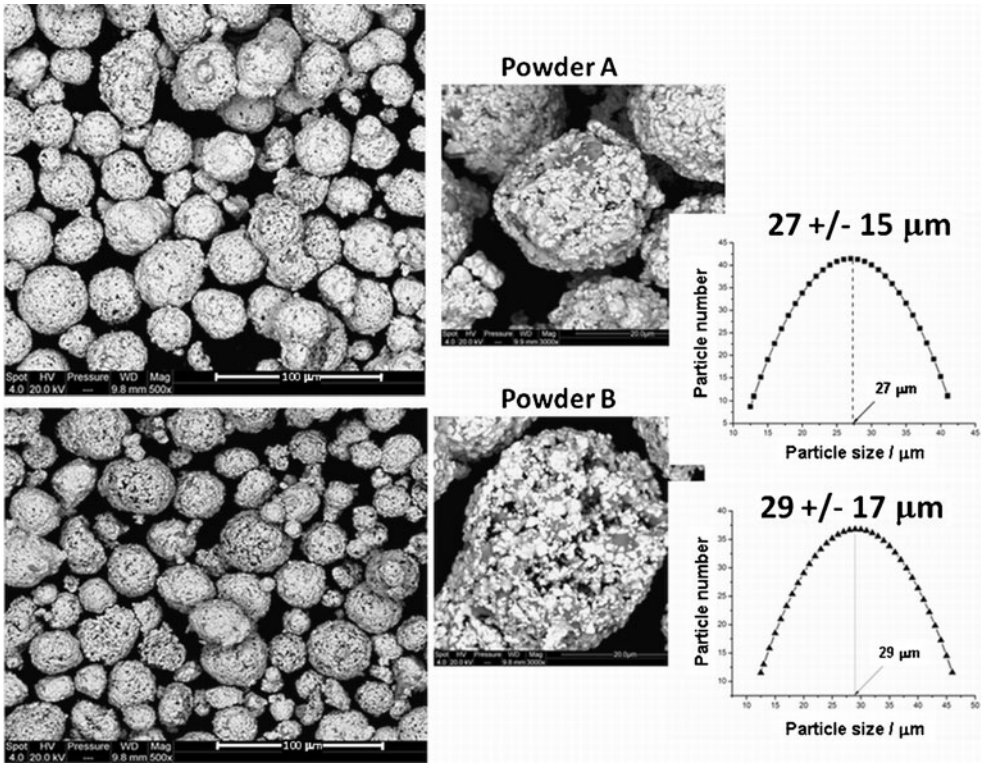


**Fig. 1** SEM observations and particle size distribution in powder A and B

27 µm and powder B had a grain size ranging from 15 to 45 µm with an average grain size of about 29 µm. Distribution of particle sizes is quite similar between these two powders. These values, deduced from the statistical approach, are in perfect agreement with the supplier data presented in Table 1 resulting from either sieving or scalping techniques. Usual classifications of particle sizes according to these techniques are −38+10 µm for powder A and −45+15 µm for powder B, meaning that the particle sizes detected by these techniques range respectively between 10 and 38 and 15 and 45 µm. For both powders, WC particles have angular shapes with grain size between 2 and 5 µm. Distribution of the WC particles are quite homogenous in the agglomerated spherical particles. Few of these particles were broken permitting to assess to the internal microstructure.

Figure 2 shows the X-ray diffraction patterns of as-sprayed WC-CoCr and WC-CoCrNi coatings deposited by HVOF process. WC is the major phase detected whereas few diffraction peaks associated to $W_2C$ phase are also observed in all deposited coatings. Presence of the $W_2C$ peaks indicates a very weak decarburization of WC taking place during the coating process, as it was reported for cermet coatings developed from HVOF thermal spray process [4, 27–31]. We also observed a very little peak corresponding to brittle η-phase $M_{12}C$ ($Co_6W_6C$); this phase could appear due to the dissolution of C in the metallic binder [31]. Formation of the mixed carbide could induce brittleness of the samples.

Although notable amount of binder phase was present in the coating, XRD analysis do not permit to distinguish the presence of Co, probably due to the low crystalline order of this phase, which organization is at very short range, or even amorphous [32]. During the thermal-spray process, cooling rates of the sprayed particles are very high that could explain an amorphization of the metallic phase [15]. An amorphous phase was reported to be more interesting for corrosion resistance compared with a crystalline material [25, 33–36] due to the lack of microstructural defects that could promote localized degradation. But formation of multiple phases within the metallic matrix due to dissolution of carbon and tungsten could contribute

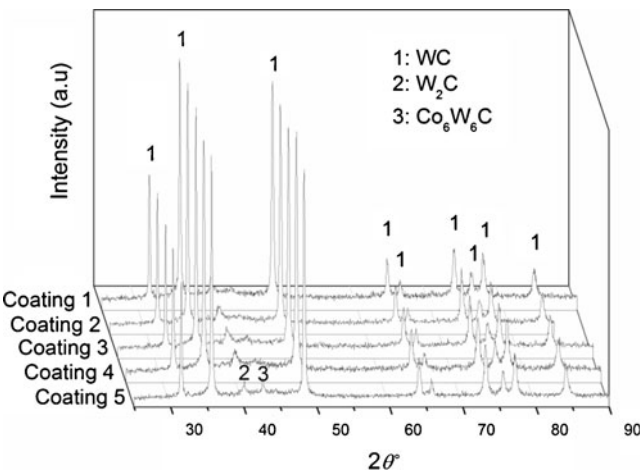


**Fig. 2** XRD patterns of as-sprayed tungsten carbide-based coatings

to a non-uniform degradation of the metallic binder as reported by Perry et al. [13].

## Electrochemical impedance measurements

Most multilayered coating systems composed of a substrate and coating layers are sensitive to galvanically induced local corrosion [33]. Galvanically induced corrosion leads to a severe attack as soon as the coating layer is perforated. This corrosion process is extremely severe for coated systems due to the high current density localized at the defect and result from a large ratio between the surface areas of the cathodic outer surface and the anodic defect.

Electrochemical impedance measurements were performed at different hours of immersion in simplified artificial seawater. EIS data were analyzed by using the equivalent circuits reported in the literature for coated metal [37].

Figure 3 shows the evolution of Nyquist and Bode diagrams after different hours of immersion for coating 1 that was deposited using the standard deposition parameters. These results show the presence of a single capacitive loop after 1 h of immersion, indicating a single time constant that can be attributed to the charge transfer resistance in parallel with the double-layer capacitance. The fact that only one time constant is obtained may be due to the short exposure time [38, 39]. We can assume that the infiltration electrolyte has not cross over the 250 μm thick of the coating and does not reach the steel substrate. So, during the first hours of immersion, the electrochemical characteristics deduced from EIS measurements could be mainly associated to a faradic process that involves the coating reactivity. However, capacitive loop diameter values are not so high, around few kΩ $cm^2$. Some authors have observed uniform dissolution of the Co matrix until corrosive media at pH close to that of seawater [15]. But it is also reported that incorporation of chromium effectively permits to reduce this phenomenon. Furthermore, some authors have also suggested the presence of coupling effect between WC particles and the metallic matrix [13, 17, 18]. These coupling effects induce an anodic polarization of the metallic binder that could favor the dissolution or passivation of the metallic binder. According to Saha et al. [17], Nyquist diagrams in saline solution (NaCl 3.5%) of $WC\text{-}_{10}Co_4Cr$ coatings deposited onto low-alloy steel present only one capacitive loop, with a charge transfer resistance around 1,500 to 1,900 Ω $cm^2$. The important thickness of the coatings (approximately 530 μm) delays the infiltration of electrolyte, and the electrochemical characteristic was affected by the coating behavior [17]. At the beginning of the immersion, the electrochemical behavior is associated to the coating oxidation and probably passivation of the metallic binder due to the weakly alkaline pH of seawater. In fact, SEM observations of the corroded samples after immersion tests (not presented) have revealed the presence of local oxidation of the binder, but these analyses do not suggest uniform dissolution of the metallic binder.

After 4 h of immersion, the shape of Nyquist diagram is changed, and two time constants occurring respectively at the middle and low frequencies are observed. The diameter of the capacitive loop observed at the middle frequencies is larger than the latter determined at the beginning of the immersion, and a second time constant is observed for lower frequencies which can be related to a Warburg element. Indeed, this evolution can be directly linked to the infiltration of electrolyte through the pores that provokes localized corrosion of the steel substrate. The capacitive loop observed at middle frequencies could be mainly associated to the steel dissolution through the coating defects, the electrochemical behavior of the coating becoming partially masked during the displacement of the corrosion potential when degradation progresses. As the sizes of the pores are very small and depend directly on the morphology and microstructure of the coatings, the formation of steel corrosion products permits to partially seal

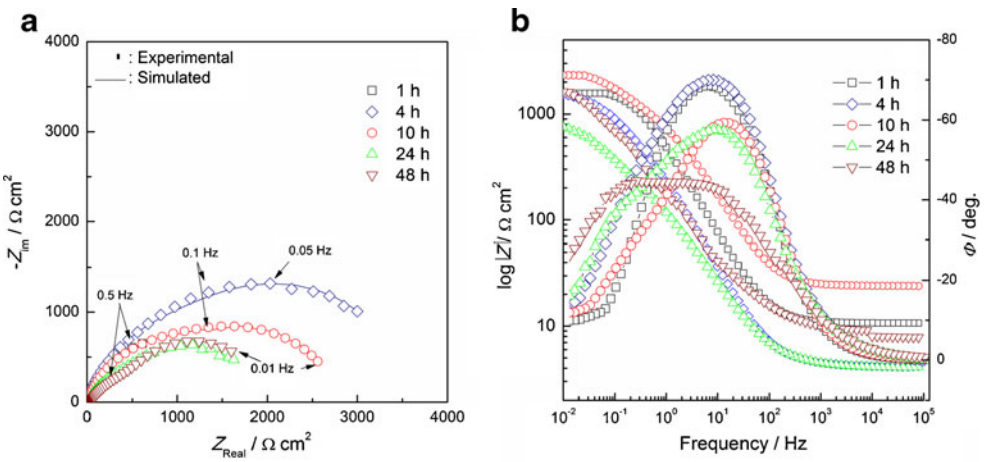


**Fig. 3** EIS data for coating 1 at different exposure time in simplified artificial seawater: **a** Nyquist diagram; **b** Bode diagram

them. But, these corrosion products are very powdery, not adherent and allow the electrolyte to access the substrate. Diffusion of ionic species will provoke a partial hydrolysis of the corrosion products increasing the aggressiveness of the electrolyte inside the pores. So, the diameter of the capacitive loop at the middle frequencies gradually decreases during the immersion, as observed in Fig. 3a, indicating that the localized degradation of steel is accelerated due to the change of electrolyte aggressiveness inside the pores combined to the galvanic coupling that may exist between the coating and the substrate.

Figure 4 shows the Nyquist and Bode diagrams of all cermet coatings, compared with the steel substrate, after different hours of immersion (1, 10, and 48 h) in simplified artificial seawater.

During the immersion, electrolyte may infiltrate inside the pores all along the coating thickness before reaching the substrate. So, at the beginning of the immersion, the electrochemical behavior is quite associated to the intrinsic coating properties. All the composite coatings present a resistive behavior corresponding to one capacitive semicircle. Coating 5 presents the highest resistance at the beginning of the immersion compared with other configurations. Coatings 1, 2, and 4 present quite similar behaviors whereas coating 3 seems to be less protective. Indeed, coating 5 presents nickel incorporation that enhanced the intrinsic behavior of the metallic matrix, whereas other coatings (1 to 4) have quite similar composition for the matrix. This may explain the high impedance values observed for this coating. Anyway, it can be underlined that the electrochemical parameters associated to the intrinsic corrosion behavior of the coating are not so different from those of the steel substrate, so the separation of each contribution when electrolyte reaches the substrate is impossible.

At the beginning of immersion, the reduction of the gun traverse velocity (coating 2) or the reduction of the powder feed rate (coating 4) during the deposition process, seems to not affect significantly the intrinsic corrosion behavior of the coatings compared with coating 1 deposited with standard parameters. However, the modification of the flame temperature during the deposition process (coating 3) seems to drastically affect the coating reactivity that could be associated to a modification of microstructure. It was reported that the corrosion behavior of the composite coatings WC-CoCr was mainly dependent on the formation of micro-galvanic cells between WC particles and the CoCr binder [17, 18]. The distribution of WC particles inside the metallic binder plays an important role on the magnitude of the coating degradation. So, we can suppose that modification of the deposition parameters associated to coatings 2 and 4 leads only to slight differences on the distribution of WC particles whereas the reduction of the flame temperature would favor heterogeneous distribution of WC particles that amplifies the galvanic degradation of the metallic binder.

After 10 h of immersion, the shape of Nyquist and Bode diagrams of the coated steels are quite similar. Diagrams are composed of two time constants, a capacitive loop at middle frequencies that can be attributed to the steel dissolution through coating defects and at low frequencies a diffusion mechanism is involved. Coatings 1 and 4 present the highest resistance values compared with coatings 2, 3, and 5 that have quite similar behavior after 48 h of immersion. In artificial seawater, WC-CoCr coatings are nobler than steel substrate, so corrosion behavior is mainly dependent on porosity rate and interconnection of porosity through the coatings. So differences in corrosion behavior between coatings 1 to 4 are correlated to variations of pore density and distribution. Surface morphological observations (not presented) of the as-sprayed coatings have revealed important heterogeneities of distribution of WC particles on coatings 3 and slight heterogeneities in case of coating 2 whereas these distributions on coatings 1 and 4 were more homogeneous. Concerning coating 5, incorporation of nickel ennobles the potential of the binder phase that worsen the galvanic coupling between steel and coating. So even if the porosity distribution is quite similar compared with the other configurations, the galvanic corrosion is amplified and the resistance of coating 5 is lowered.

Two different models of equivalent electrical circuit are used for the fitting of the experimental EIS data (Fig. 5). Figure 5a corresponds to the equivalent circuit that correctly fits the EIS data linked to the intrinsic corrosion behavior of the coatings in aerated and stirred seawater. This circuit is composed of the solution resistance $R_s$, the charge transfer resistance of the coatings/solution interface $R_{ct(coating)}$ and the double-layer capacitance $C_{dl(coating)}$ represented by a constant phase element (CPE) [40]. After 4 h of immersion, the shapes of Nyquist diagrams are changed and Fig. 5b present the equivalent electrical circuit that correctly fits the EIS data linked to the dissolution of steel substrate through the coating defects. The circuit is composed of the solution resistance $R_s$, the charge transfer resistance of the steel/solution interface through the coating defects $R_{ct(steel)}$, the double-layer capacitance $C_{dl(steel)}$ represented by a CPE [40] and the Warburg diffusion process of electrolyte and oxygen. The corrosion rate is limited by the slow diffusion of the electrolyte and the oxygen through the defects in the coating. Therefore a Warburg element ($W_s$) should be adopted in series with the charge transfer resistance (Fig. 5) to account for the finite length of the diffusion pathway. This diffusion element is characterized by two parameters, the diffusion resistance $R_{d,}$ and the time constant for diffusion through the distance

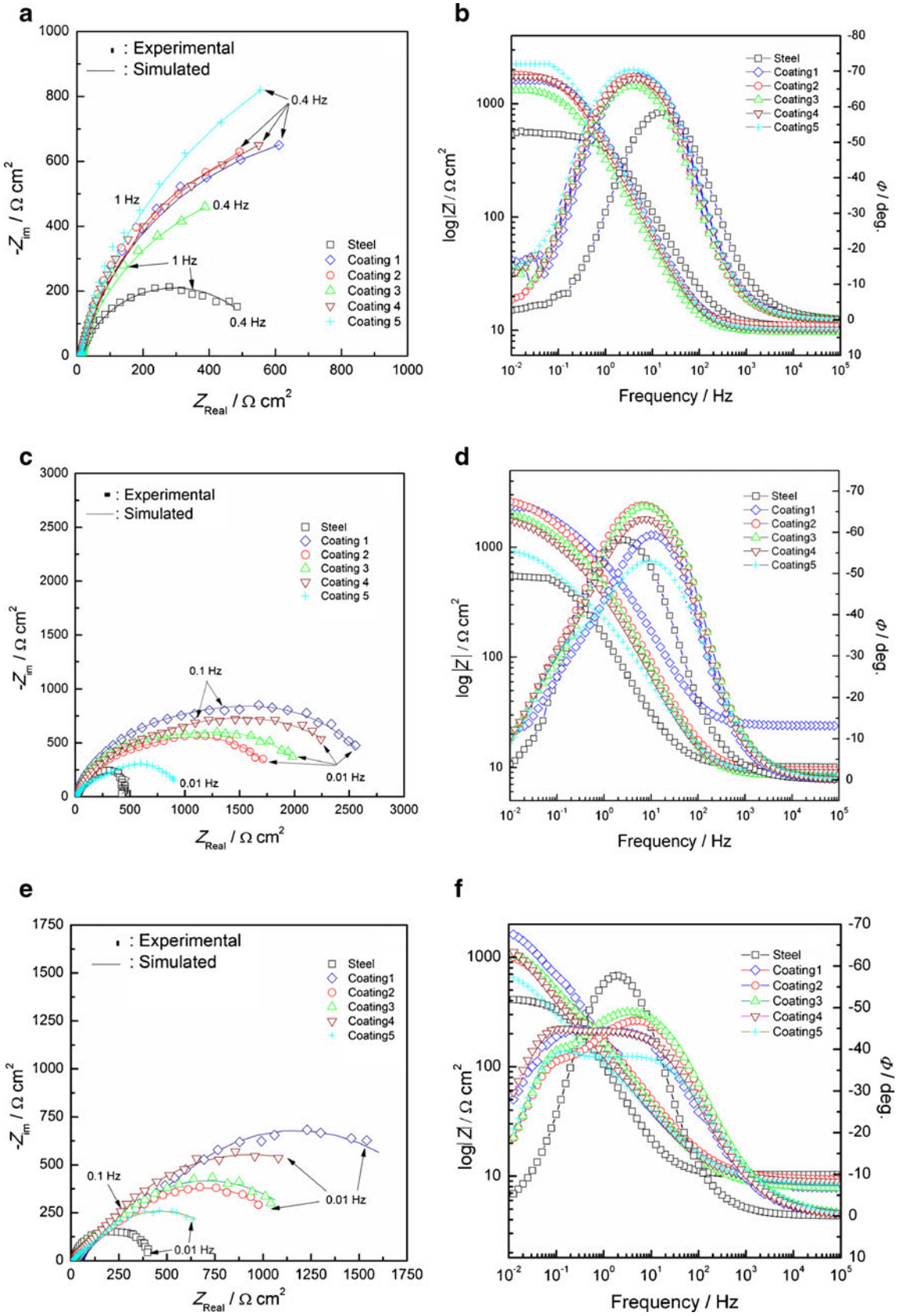


**Fig. 4** EIS data for substrate and all coatings at different exposure time in simplified artificial seawater: **a** Nyquist diagram after 1 h; **b** Bode diagram after 1 h; **c** Nyquist diagram after 10 h; **d** Bode diagram after 10 h; **e** Nyquist diagram after 48 h; **f** Bode diagram after 48 h

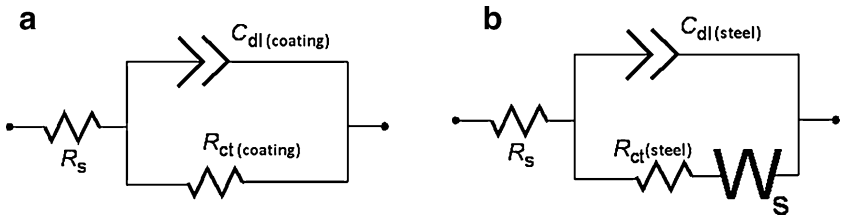


**Fig. 5** **a** Equivalent circuit to fit the electrochemical impedance data of the mild steel substrate and coatings until 4 h of exposure time. **b** Equivalent circuit used for fitting the electrochemical impedance data of the coated samples

δ corresponding to the average thickness of the as-sprayed coating : $T_d=\delta^2/D$. $D$ represents the diffusion coefficient of the considered species. The fitting is achieved using the $Z_{view}$ software and a good correlation was observed for all the EIS diagrams. All the electrochemical parameters deduced from the fitting of the experimental data using the equivalent electrical circuit described in Fig. 5 are presented in Table 4. As it can be seen, the error parameter $\chi^2$ is quite low for all fitting operations. Figure 6 presents the evolution of different electrochemical parameters deduced from the fitting of the EIS diagrams associated to the charge transfer reactions ($R_{ct}$ and time constant $\tau_F$) and to the diffusion mechanism ($R_D$ and time constant $\tau_D$) versus the immersion time. It must be noticed that time constants $\tau_F$ were calculated using true capacitances $C_{dl}$ obtained from Brug's relation [40].

Figure 6a, b shows the evolution of the charge transfer resistance $R_{ct}$ which is inversely proportional to the corrosion rate, deduced from EIS measurements in the middle frequency range, as a function of immersion time. For coated steels, initial values of $R_{ct}$ are quite higher than that of steel and correspond to the intrinsic behavior of the composite coatings as presented in Fig. 5a. Except for coating 5 whose composition is different from the other configurations, the time constants $\tau_F$ (Fig. 6c) associated to the charge transfer reaction are quite similar indicating that same electrochemical mechanism is involved. Up to approximately 4 h of immersion, the slight increase of the charge transfer resistance is attributed to the passivation of the metallic binder in contact with seawater. When the electrolyte infiltration reaches the steel substrate, degradation of steel becomes the predominant mechanism due to the galvanic coupling with the coatings. Figure 6a, b shows two different evolutions of the $R_{ct}$ values when the electrolyte reaches the substrate. Up to 10 h of immersion, an increase of the transfer resistance is observed for coatings 1 and 4. As corrosion becomes localized at the defects of the coatings, steel corrosion products may accumulate and partially seal the pores. The time constants $\tau_F$ of these coatings increases and reach values during this immersion period higher than the other configuration for which a drastic decrease is observed. Effectively, the morphology, distribution, or interconnection of pores for coatings 2, 3, and 5 seem to limit the sealing effect of the corrosion products. After 10 h of immersion, the charge transfer resistances $R_{ct}$ of coatings 1 and 4 drastically decrease as previously observed for the other configurations. Accumulation of metallic ions inside the pores due to the dissolution of the steel substrate favors the diffusion of anions like chloride, in order to restore the balance of electrical charges that will modify the aggressiveness of the solutions. The ionic species diffusion that is created between the confined electrolyte inside the pores and the bulk solution may favor the modification of the electrolyte composition and chemistry inside the pores that would induce local acidification. This mechanism is strongly dependent on the microstructure of the coatings (size, shape, and density of open porosity) and on the degradation amplification of the less noble material in the galvanic coupling between two conductive materials. Comparatively to nitride coatings or multilayer nitride based coatings [37] whose electrochemical parameters are quite separated from steels ones, EIS diagrams permit to evaluate the coating properties and the evolution of the pore electrolyte resistance during immersion. The electrochemical parameters of the cermet coatings, mainly dependent on the reactivity of the metallic phase are not more distinguishable in the EIS diagrams when steel localized degradation occurs. The decrease of $R_{ct}$ indicates then that the shape of the pores and/or the interconnection of porosity do not permit to confer an effective sealing. So, $R_{ct}$ gradually decreases during the immersion to reach values close to those of the steel substrate after 48 h of immersion.

For coating 5, initial values of $R_{ct}$ is effectively higher compare with the other configurations but rapidly the $R_{ct}$ values decrease drastically, reaching values smaller than those of the steel substrate. Incorporation of nickel has a detrimental effect on the galvanic corrosion occurring between the substrate and the coating, so dissolution of the substrate is more intense through the defects of the coating, and the corrosion products do not modify the diffusion of species through the pores as observed on Fig. 6b.

Figure 6d, e shows the evolution of diffusion resistance $R_D$ and time constant $\tau_D$ deduced from EIS measurements in the low frequency range. It can be seen that a noticeable decrease of $R_D$ can be detected after the first hours of immersion for coatings 2, 3, 4, and 5 while there is a slight increase for coating 1. After 15 h, the $R_D$ values reach a constant value for all coatings except for coating 4 where

**Table 4** Electrochemical parameters deduced from the fittings of the EIS experimental data after different immersion times

| | Hours | 0.5 | 1.0 | 2.0 | 4.0 | 6.0 | 10.0 | 16.0 | 24.0 | 36.0 | 48.0 |
|---|---|---|---|---|---|---|---|---|---|---|---|
| Steel | $R_s$/Ω cm$^2$ | 11.02 | 11.13 | 11.4 | 10.6 | 10.5 | 10.33 | 10.52 | 10.54 | 10.32 | 10.52 |
| | CPE-$Y_0$/mF cm$^{-2}$ s$^{n-1}$ | 0.000301 | 0.000304 | 0.000337 | 0.000895 | 0.00118 | 0.001427 | 0.001538 | 0.001615 | 0.001812 | 0.0019677 |
| | CPE-$n$ | 0.8 | 0.812 | 0.827 | 0.778 | 0.789 | 0.79155 | 0.8035 | 0.816 | 0.828 | 0.827 |
| | $C_{dl}$/μF cm$^{-2}$ | 72 | 81 | 105 | 236 | 363 | 468 | 559 | 641 | 789 | 870 |
| | $R_{ct}$/Ω cm$^2$ | 553 | 569 | 532 | 585 | 486 | 697 | 626 | 475 | 429 | 411 |
| | $\tau_F$/ms | 40 | 46 | 56 | 138 | 176 | 326 | 350 | 305 | 338 | 357 |
| | $\chi^2$ | 0.00091 | 0.0007 | 0.0013 | 0.00064 | 0.00088 | 0.000277 | 0.00031 | 0.00061 | 0.00055 | 0.00033 |
| Coating 1 | $R_s$/Ω cm$^2$ | 11.2 | 11.32 | 10.7 | 10.5 | 15 | 25 | 23.7 | 18.18 | 25.6 | 41 |
| | CPE-$Y_0$/mF cm$^{-2}$ s$^{n-1}$ | 0.000303 | 0.000374 | 0.000504 | 0.000334 | 0.000306 | 0.000359 | 0.00042 | 0.000482 | 0.000636 | 0.000967 |
| | CPE-$n$ | 0.891 | 0.867 | 0.815 | 0.86 | 0.871 | 0.838 | 0.822 | 0.81 | 0.791 | 0.723 |
| | $C_{dl}$/μF cm$^{-2}$ | 151 | 162 | 154 | 133 | 138 | 144 | 154 | 158 | 212 | 274 |
| | $R_{ct}$/Ω cm$^2$ | 1,367 | 1,745 | 2,241 | 2,602 | 2,688 | 1,774 | 1,155 | 889 | 752 | 619 |
| | $\tau_F$/ms | 206 | 282 | 345 | 346 | 370 | 255 | 178 | 140 | 160 | 170 |
| | W-$R_D$/Ω cm$^2$ | – | – | – | 965 | 1,093 | 1,215 | 1,255 | 1,383 | 1,414 | 1,386 |
| | W-$T$/s | – | – | – | 10.3 | 9.5 | 9.5 | 9.38 | 9.51 | 10.01 | 10.17 |
| | W-$n$ | – | – | – | 0.5 | 0.5 | 0.5 | 0.5 | 0.5 | 0.5 | 0.5 |
| | $\chi^2$ | 0.0011 | 0.00349 | 0.00069 | 0.00022 | 0.00018 | 0.00633 | 0.00085 | 0.00079 | 0.00094 | 0.000373 |
| Coating 2 | $R_s$/Ω cm$^2$ | 11.78 | 12.6 | 12.4 | 10.58 | 10.4 | 9.63 | 9.4 | 10 | 9.4 | 9.7 |
| | CPE-$Y_0$/mF cm$^{-2}$ s$^{n-1}$ | 0.000343 | 0.000436 | 0.000667 | 0.000411 | 0.000324 | 0.000357 | 0.000496 | 0.00066 | 0.000997 | 0.001318 |
| | CPE-$n$ | 0.881 | 0.88 | 0.82 | 0.835 | 0.861 | 0.838 | 0.793 | 0.753 | 0.71 | 0.671 |
| | $C_{dl}$/μF cm$^{-2}$ | 163 | 214 | 232 | 140 | 129 | 119 | 122 | 127 | 147 | 154 |
| | $R_{ct}$/Ω cm$^2$ | 1,320 | 1,813 | 1,751 | 1,385 | 1,661 | 1,498 | 834 | 722 | 508 | 412 |
| | $\tau_F$/ms | 215 | 388 | 407 | 194 | 214 | 178 | 102 | 91 | 75 | 63 |
| | W-$R_D$/Ω cm$^2$ | – | – | – | 2,060 | 1,701 | 1,150 | 770 | 788 | 727 | 786 |
| | W-$T$/s | – | – | – | 4.1 | 5.88 | 6.49 | 5.4 | 5.85 | 5.65 | 5.7 |
| | W-$n$ | – | – | – | 0.5 | 0.5 | 0.5 | 0.5 | 0.5 | 0.5 | 0.5 |
| | $\chi^2$ | 0.00148 | 0.00149 | 0.00356 | 0.000653 | 0.000383 | 0.000437 | 0.000484 | 0.000353 | 0.000303 | 0.000409 |
| Coating 3 | $R_s$/Ω cm$^2$ | 10.7 | 11.15 | 9.8 | 9.35 | 9.1 | 8.6 | 8.5 | 8.4 | 8.1 | 8.48 |
| | CPE-$Y_0$/mF cm$^{-2}$ s$^{n-1}$ | 0.000408 | 0.000593 | 0.000927 | 0.000347 | 0.000336 | 0.000396 | 0.000651 | 0.000903 | 0.00119 | 0.00145 |
| | CPE-$n$ | 0.883 | 0.855 | 0.759 | 0.867 | 0.867 | 0.841 | 0.777 | 0.735 | 0.703 | 0.674 |
| | $C_{dl}$/μF cm$^{-2}$ | 198 | 253 | 208 | 144 | 138 | 135 | 146 | 155 | 166 | 171 |
| | $R_{ct}$/Ω cm$^2$ | 1,128 | 1,404 | 1,899 | 1,378 | 1,591 | 1,157 | 657 | 643 | 548 | 494 |
| | $\tau_F$/ms | 224 | 355 | 395 | 198 | 220 | 156 | 96 | 99 | 91 | 85 |

**Table 4** (continued)

| | Hours | 0.5 | 1.0 | 2.0 | 4.0 | 6.0 | 10.0 | 16.0 | 24.0 | 36.0 | 48.0 |
|---|---|---|---|---|---|---|---|---|---|---|---|
| | W-$R_D$/Ω cm$^2$ | – | – | – | 1,441 | 1,049 | 921 | 730 | 745 | 752 | 829 |
| | W-$T$/s | – | – | – | 7.4 | 8.5 | 9 | 6.3 | 6.4 | 5.5 | 5.9 |
| | W-$n$ | – | – | – | 0.5 | 0.5 | 0.5 | 0.5 | 0.5 | 0.5 | 0.5 |
| | $\chi^2$ | 0.002162 | 0.00416 | 0.00511 | 0.000729 | 0S.000568 | 0.000473 | 0.000354 | 0.000147 | 0.000118 | 0.000131 |
| Coating 4 | $R_s$/Ω cm$^2$ | 11.51 | 11.45 | 9.52 | 10 | 10 | 9.4 | 9.4 | 9.4 | 8.62 | 8.5 |
| | CPE-$Y_0$/mF cm$^{-2}$ s$^{n-1}$ | 0.000306 | 0.000414 | 0.000588 | 0.00035 | 0.000307 | 0.000477 | 0.000592 | 0.000768 | 0.00152 | 0.00219 |
| | CPE-$n$ | 0.881 | 0.863 | 0.784 | 0.864 | 0.886 | 0.825 | 0.797 | 0.76 | 0.662 | 0.605 |
| | $C_{dl}$/μF cm$^{-2}$ | 143 | 177 | 141 | 144 | 146 | 151 | 157 | 161 | 165 | 161 |
| | $R_{ct}$/Ω cm$^2$ | 1,793 | 1,874 | 2,579 | 2,662 | 2,501 | 873 | 772 | 728 | 641 | 602 |
| | $\tau_F$/ms | 256 | 331 | 363 | 382 | 365 | 132 | 121 | 117 | 106 | 97 |
| | W-$R_D$/Ω cm$^2$ | – | – | – | 1,648 | 1,201 | 907 | 983 | 1,131 | 1,233 | 1,578 |
| | W-$T$/s | – | – | – | 4 | 3.6 | 6.2 | 7 | 7 | 7 | 6.8 |
| | W-$n$ | – | – | – | 0.5 | 0.5 | 0.5 | 0.5 | 0.5 | 0.5 | 0.5 |
| | $\chi^2$ | 0.00053 | 0.0018 | 0.000539 | 0.000398 | 0.000185 | 0.000583 | 0.000566 | 0.000431 | 0.000391 | 0.000219 |
| Coating 5 | $R_s$/Ω cm$^2$ | 11.5 | 12 | 11 | 9.3 | 9 | 8.9 | 8.8 | 8.8 | 8.62 | 8.2 |
| | CPE-$Y_0$/mF cm$^{-2}$ s$^{n-1}$ | 0.000298 | 0.000364 | 0.000563 | 0.000539 | 0.000676 | 0.000781 | 0.000956 | 0.00117 | 0.00181 | 0.002364 |
| | CPE-$n$ | 0.889 | 0.888 | 0.808 | 0.791 | 0.762 | 0.749 | 0.722 | 0.697 | 0.627 | 0.583 |
| | $C_{dl}$/μF cm$^{-2}$ | 147 | 183 | 168 | 132 | 137 | 147 | 150 | 158 | 149 | 137 |
| | $R_{ct}$/Ω cm$^2$ | 2,749 | 2,788 | 2,752 | 624 | 501 | 393 | 355 | 247 | 232 | 199 |
| | $\tau_F$/ms | 403 | 511 | 462 | 83 | 68 | 58 | 53 | 39 | 35 | 27 |
| | W-$R_D$/Ω cm$^2$ | – | – | – | 978 | 633 | 557 | 584 | 665 | 610 | 714 |
| | W-$T$/s | – | | – | 4.5 | 4.5 | 4.5 | 4.5 | 4.5 | 4.4 | 5.7 |
| | W-$n$ | – | – | – | 0.45 | 0.5 | 0.5 | 0.48 | 0.45 | 0.5 | 0.5 |
| | $\chi^2$ | 0.000407 | 0.0012 | 0.000768 | 0.000402 | 0.000359 | 0.000196 | 0.000113 | 0.000209 | 0.000189 | 0.000136 |

Up to 4 h of immersion, electrochemical parameters are linked to the composite coating characteristics (deduced from equivalent circuit, Fig. 5a) and for longer immersion periods, the electrochemical parameters are associated to steel degradation through the coating defects (deduced from equivalent circuit, Fig. 5b)

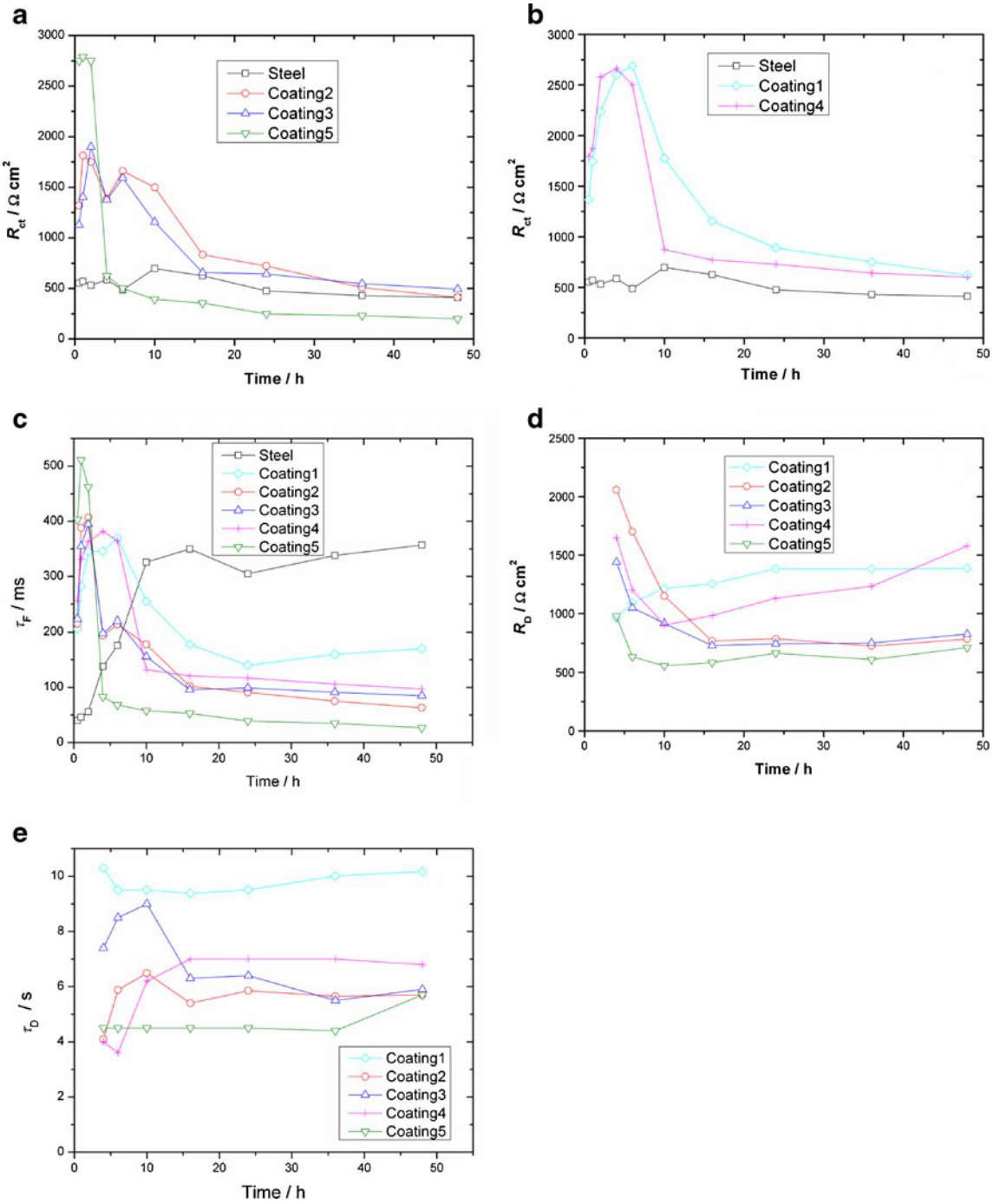


**Fig. 6** EIS data for substrate and coatings at different exposure time in artificial seawater: **a** Resistance charge transfer for substrate, coating 2, coating 3, and coating 5; **b** Resistance charge transfer for substrate, coating 1 and coating 4; **c** time constant $\tau_F$ associated to the charge transfer reactions, **d** Warburg diffusion resistance, and **e** diffusion time constant $\tau_D$

$R_D$ values still increase. The behavior observed for coatings 1 and 4 can be related to the homogeneous distribution of chemical phases (WC particles and CoCr binder) for both coatings, as previously mentioned. Finally, after 48 h immersion time, it can be seen that $R_{ct}$ and $R_D$ values of coating 1 and coating 4 are higher than other coatings, probably due to a less important porosity rate than other configurations, or by the pore geometry configuration that favors partial sealing during the aging of the coated samples. Time constant evolutions (Fig. 6e) are not so relevant compare with the diffusion resistance evolution, because the evolution of this parameter is very dependant on the shape, interconnection paths between porosities. Anyway, $\tau_D$ evolutions confirm after extended immersion

tests that coatings 1 and 4 present the best corrosion behavior in seawater.

Evolution of electrochemical behavior of the coated steels in artificial seawater is directly link to variations of metallurgical states in the as-sprayed coatings. Modification of the deposition parameters may affect the properties of the as-sprayed coatings through evolution of the density and/or porosity and detectable phases inside the coatings [41]. Three parameters were reduced compare with the standard deposition mode, as reported in Table 2.

Gun transverse velocity was reduced during the synthesis of coating 2. This parameter affects the number of spray passes that are necessary for the formation of a layer. The coating is built through cumulative layers until reaching the required thickness. A reduction of the transverse parameter will mainly modify the amount of matter deposited in a single pass without affecting the microstructure (distribution of the components WC particles/metallic binder). At the beginning of the immersion, intrinsic corrosion behavior of coating 2 is normally similar to that of the reference coating 1 since distributions of WC particles are quite similar. The amount of deposited matter is more important when this parameter is reduced, so the number of sublayers for a constant coating thickness is decreased and it was reported that porous structures are then favored [41]. Fitting parameters presented in Table 4 after 4 h of immersion suggest that the surface porosity for coating 2 is narrow that could explain the important value of the diffusion resistance. But as the number of sublayers is reduced, interconnected porosity are certainly much more important in coating 2, increasing then the number of infiltration paths for electrolyte towards steel substrate and favoring the diffusion through the coating.

Flame temperature and powder feed rate were reduced during the synthesis of coatings 3 and 4, respectively. It was reported that both parameters influence the particle in-flight properties [3, 42, 43]. Zhao et al. [42] had reported that the increase of gas flow rate increases strongly temperature and velocity of particles. Same trends were observed when decreasing the powder feed rate. The amount of energy transferred to the powders are more important, and the higher temperature of the particles favors a better melting that permits the formation of more homogeneous and compact coatings, built through accumulation of thinner sublayers [3, 43]. Indeed, coating porosity seems to decrease with increasing particle temperature, same trends were observed but in less extend when increasing particle velocity [42]. So, we can expect that the reduction of the flame temperature (coating 3) will modify the metallurgical state of the coating, maybe affecting the composition by incorporation of un-melted particles for instance. Coating 3 presents effectively a more important intrinsic reactivity compare with other configurations during the first hours of immersion that could be associated to composition variation leading to heterogeneous distribution of WC particles and metallic binder. Reduction of powder feed rate (coating 4) induces a better melting of powder particles and increases the particle velocity that favors a homogeneous distribution of WC particles and metallic binder. So the intrinsic corrosion behavior is higher compared with the other coatings deposited from powder A. Then, the reactivity of coating 4 is quite similar to that of the reference coating 1. However, density, shape, size, and interconnection of porosity should be different between these both coatings that could explain the differences in diffusion resistance evolution observed between 4 and 10 h of immersion.

Powder composition was also examined using a commercial powder containing a small amount of nickel (powder B). Powder morphology and characteristics (density, particle sizes, porosity, etc.) affect the properties of the as-sprayed coatings [41]. Powders A and B present quite similar morphological characteristics (Fig. 1) and similar particle size distributions. Standard deposition parameters were used for the deposition of coating 5. Incorporation of nickel in the composition of the particles can affect the melting temperature but also the available time for chemical reactions inside the flame influencing the coating microstructure. Electrochemical parameters deduced from the EIS measurements like $R_{ct}$ and $R_D$ in Fig. 6a, c underline that coating 5, which presents the highest intrinsic corrosion resistance, suffers from the presence of an important density of defects.

## SEM cross-section and OM observations of corroded as-sprayed coated samples

Optical microscopy (OM) studies of the corroded samples after EIS measurements indicate different types of defects for all coatings. Figure 7 presents optical observations in polarized light mode respectively of the corroded surface of coatings 2 and 5 after extended immersion tests. Emergence of the corrosion product through few defects is observed during immersion of the as-sprayed WC-CoCr coatings, and it can be seen that new corroded zones progressively appear during immersion suggesting interconnection between defects through the as-sprayed coatings. Perry et al. [13] announced that low porosity rate of HVOF coatings, reported below 3–5%, would not favor porosity interconnection and so would not control the corrosion behavior of the as-coated samples, but our observations are not in agreement with that. OM observations reveal the presence of three different types of corrosion products emerging on or spread over the sample surface. μ-Raman spectroscopy was used in order to characterize the nature of the corrosion products detected on the surface of the

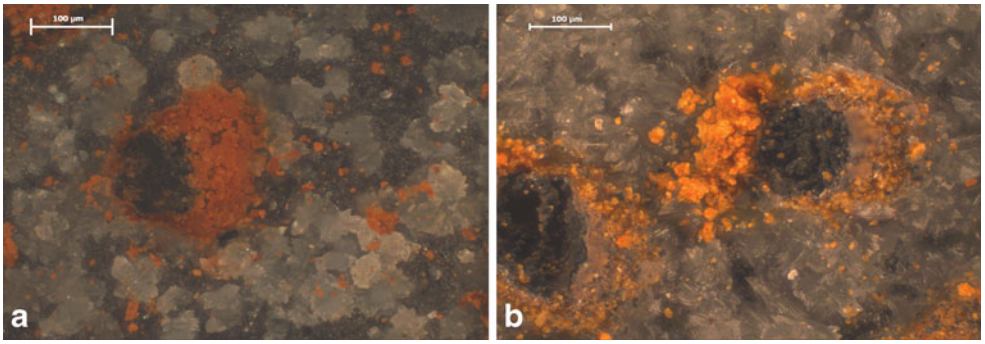


**Fig. 7** OM observations after extended immersion of coating 1 (**a**) and coating 5 (**b**)

corroded samples. Raman spectra associated to the degradation products typically encountered on the exposed surface to the corrosive solution are presented in Fig. 8. Figure 8a presents different vibrational bands at 246, 296, 375, 521, 641, and 1,293 $cm^{-1}$ that are typically attributed to lepidocrocite (γ-FeOOH) [44]. These powdery steel corrosion products are mainly present on the surface of the open defects. Two supplementary bands are present around 1,365 and 1,395 $cm^{-1}$ and were punctually detected on the surface of the samples. According to the literature, these bands could be associated to the presence of carbon-rich phases included into the metallic binder and coming from the WC decarburization occurring during the deposition stage [45]. Figure 8b presents different vibrational bands corresponding to darkish degradation products close to the boundary between the open defects and the coating surface. Bands at 360, 482, and 579 $cm^{-1}$ are characteristic to the magnetite phase that is often observed during the steel degradation in seawater [46]: $Fe_{3-x}O_4$. The steel corrosion products come from the localized substrate degradation and diffusion of iron species through the coating thickness. The bands at 152, 206, and 1,084 $cm^{-1}$ correspond to a carbonate based product. Figure 8c details all the peaks describing this product that is ascribed to crystals of calcium carbonate. These crystals,

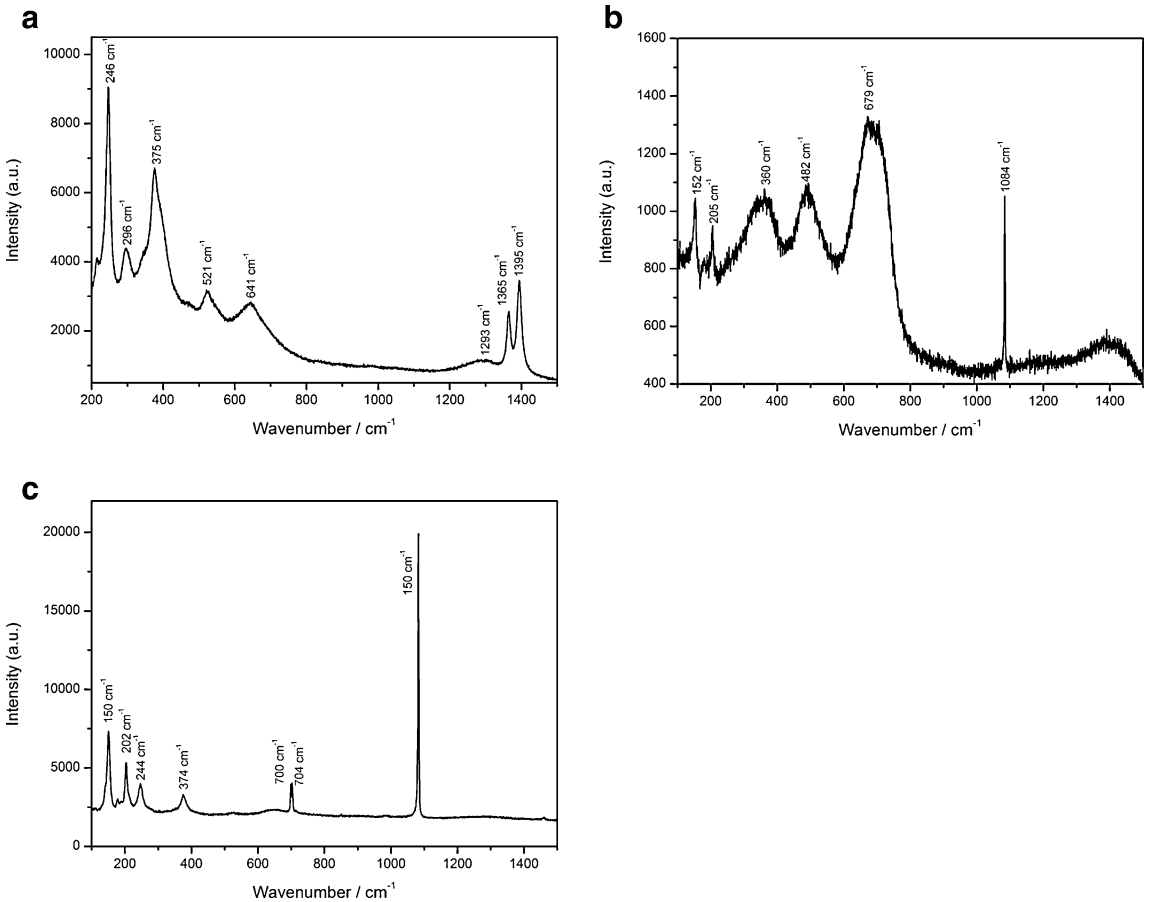


**Fig. 8** Raman spectra of the corrosion products formed on the coating samples during extended immersion tests. **a** γ-FeOOH, **b** $Fe_{3-x}O_4$, **c** $CaCO_3$

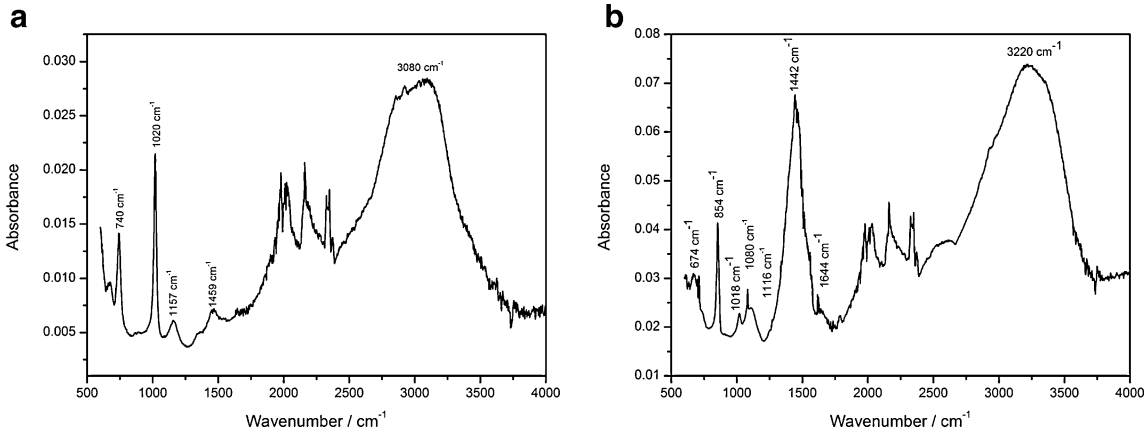


**Fig. 9** FTIR-ATR spectra characteristics of **a** γ-FeOOH and **b** $CaCO_3$

distinctly observed on the polarized light OM pictures, appear close to open defects and they are mainly composed of aragonite crystallographic form [47–49]. Doncescu et al. [47] have demonstrated that this crystallographic form of $CaCO_3$ was favored in simplified artificial seawater for low cathodic polarization due to the presence of magnesium ions that inhibited calcite and vaterite crystallographic forms.

FTIR-ATR measurements were performed on the corroded samples after extended immersion tests. Different analyses were done on each sample to confirm the results. The main phases detected by FTIR-ATR measurements are presented in Fig. 9a, b. Large bands corresponding to OH group in the 3,080–3,250 $cm^{-1}$ domain are detected. Characteristics peaks at 740, 1,020, and 1,157 $cm^{-1}$ are detected and could be associated to iron corrosion product γ-FeOOH [50] whereas peaks at 854, 1,442, and 1,644 $cm^{-1}$ are mainly associated to the aragonite crystallographic form of $CaCO_3$ [51, 52]. These complementary analyses permit to confirm the presence of iron corrosion products emerging from the open defects and formation on the coating surface of calcium carbonate due to local alkalinization resulting from the cathodic reaction occurring close to these defects.

SEM cross-section views in composition mode (backscattered electrons image) after 48 h of immersion in simplified artificial seawater (Fig. 10) shows the electrolyte infiltration through coating defects until reaching the substrate, and the formation of cavities at the substrate/coating interface. EDS analyses allowed to determine and follow the rise path of the corrosion product towards the

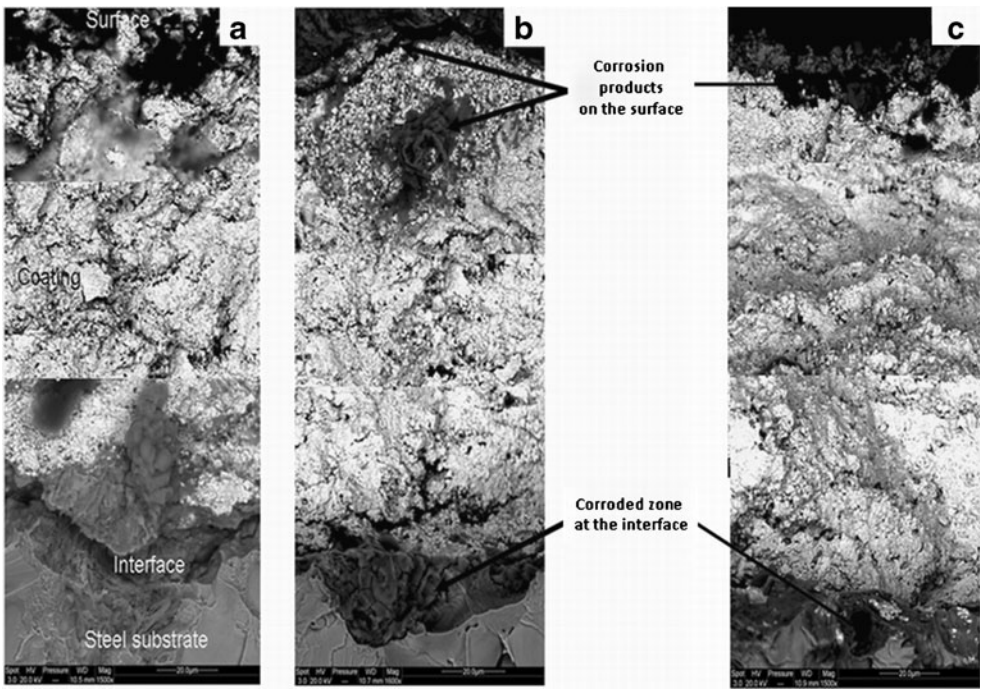


**Fig. 10** Cross-section SEM observations of samples after 48 h of immersion in seawater: **a** coating 1; **b** coating 3; **c** coating 5

surface, and so to identify in the as-sprayed coatings, the infiltration path of the solution towards the substrate.

Cross-section views of non-corroded samples, mainly in secondary electron mode, do not permit to clearly distinguish the narrow interconnected porosity of the coatings. SEM observations in backscattered electron mode (compositional view) coupled to EDS analyses were necessary to identify electrolyte infiltration paths. The cross-section analyses were performed after EIS experiments and infiltration paths were identified following the presence of iron based products from localized corrosion at the interface steel/coating until the coating surface.

Qualitatively, cross-section views are quite similar for all deposition conditions. The difference between them is the density of paths or the interconnection between porosity that could vary due to morphological modifications appearing during the change of deposition parameters. These modifications are essentially related to heterogeneity in distribution of WC particles and CoCr binder. Flame temperature and powder feed rate parameters influence the microstructure of the coatings affecting the distribution and repartition of the WC particles and metallic binders.

Diffusion parameters deduced from EIS measurements are dependent on the shape, size, and distribution of porosities inside the coatings, so directly to the distribution of components inside the coatings. The infiltration paths are very thin (few micrometers). Furthermore, shapes of the infiltration paths are very complex, few of them are linear path as presented in Fig. 10b, but others present deviations that increase the length of infiltration path. So, a delay in corrosion products emergence should be observed and could explain the appearance of new corroded zones during immersion time. Interconnection of porosity allows supplementary accesses towards the steel substrate. Diffusion of aggressive species remains effective even if the diffusion path is lengthened permitting the acceleration of the local degradation leading to the formation of cavities. Furthermore, this corrosion process is amplified by galvanic coupling between the coating (cathode) and substrate (anode).

The formation of calcium carbonate at the vicinity of the active open defects would partially block the cathodic areas that decrease the importance of the galvanic corrosion in the local dissolution of steel substrate. Anyway, evolution of the electrolyte aggressiveness inside the pores is sufficient to maintain an active dissolution of the substrate as it was confirmed by the EIS results presented after 48 h of immersion.

## Conclusions

The corrosion behavior of the as-sprayed cermet coatings deposited onto steel has been studied through the modeling of EIS spectra at different exposure times in artificial seawater solution. The results show that whatever the modification of deposition conditions, coated samples have the same corrosion mechanism which is mainly dependent on the interconnected porosity of coatings.

The EIS spectra for all coatings after 4 h of immersion presented two time constants (charge transfer and diffusion) suggesting similar corrosion. The samples developed under standard parameters (coating 1) and lower powder feed flow exhibited better corrosion resistance as compared with the other configurations.

From typical SEM images, we observed the rise of iron corrosion products on the surface for all samples, whereas the surface of the coatings remains unchanged.

The OM images shows rust covered zone corresponding to iron corrosion products which are generally surrounded by crystal of aragonite, galvanic coupling locally amplifies degradation. In the composite metallic matrix coatings, the presence of porosities and essentially interconnection between porosities may affect the electrochemical behavior of the coated samples, essentially in case of low-alloy steels. Finally, deposition parameters have a little effect on the electrochemical behavior because they mainly imply modification in microstructure and/or morphology and composition. Whatever the examined deposition conditions, infiltration of electrolyte through the defects or interconnected defects mainly control the degradation mechanism. Homogeneous distribution and repartition of WC particles and metallic binder could delay the local degradation of the steel substrate but cannot avoid it. The corrosion behavior of these as-sprayed coatings should be improved by reducing the infiltration paths (porosity) that combined to surface roughness of the coatings, induces important local degradation of steel substrate.

## References

1. Zhang SH, Cho TY, Yoan JH, Wang W, Song KO, Li MX, Loo YK, Lee GG (2008) Mater Charact 59:1412–1418
2. Collazo A, Novoa XR, Perez C (1999) Electrochim Acta 44:4289–4296
3. Magnani M, Suegama PH, Espallargos N, Dosta S, Fugivara CS, Guilemany JM, Beneditti AV (2008) Surf Coat Technol 202:4746–4757
4. Verdon C, Karimi A, Martin JL (1998) Mater Sci Eng A246:11–24
5. Villalobos-Gutiérrez CJ, Gedler-Chacón GE, La Barbera-Sosa JG, Piñeiro A, Staia MH, Lesage J, Chicot D, Mesmacque G, Puchi-Cabrera ES (2008) Surf Coat Technol 202:4572–4577
6. Aw PK, Kuan Tan AL, Phong Tan T, Qiu J (2008) Thin Solid Films 516:5710–5715
7. Bjordal M, Bardal E, Rogne T, Eggen TG (1995) Wear 186–187:508–514
8. Monticelli C, Frignani A, Zucchi F (2004) Corros Sci 46:1225–1237

9. Guilemany JM, Dosta S, Miguel JR (2006) Surf Coat Technol 201:1180–1190
10. Human AM, Exner HE (1997) Int J Ref Metals Hard Mater 15:65–71
11. Sutthiruangwong S, Mori G (2003) Int J Ref Metals Hard Mater 21:135–145
12. Konadu DS, Vander Merwe J, Potgieter JH, Potgieter-Vermarsk S, Machio CN (2010) Corros Sci 52:3118–3125
13. Perry JM, Neville A, Wilson VA, Hodgkiess T (2001) Surf Coat Technol 137:43–51
14. Schnyder B, Strössel-Sittig C, Kötz R, Hochstrasser-Kurz S, Virtanen S, Jaeggi C, Eichenberger N, Siegenthaler H (2004) Surf Sci 566–568:1240–1245
15. Monticelli C, Balbo A, Zucchi F (2010) Surf Coat Technol 204:1452–1460
16. Guilemany JM, Cabot PL, Fernandez J, Paco JM, Sanchez J (1998) Sci Eng Compos Mater 7:205–208
17. Saha GC, Khan TI (2010) Metall Mater Trans A 41:3000–3009
18. Lekatou A, Zois D, Karantzalis AE, Grimanelis D (2010) Corros Sci 52:2616–2635
19. Koga Y, Obata H, Noguchi M, Tarumi K, Ogi K (2004) Proc Int Thermal Spray Conf Osaka, Japan 10–12 may 2004.
20. Suegama PH, Fugivara CS, Benedetti AV, Fernandez J, Delgado J, Guilemany JM (2002) J Appl Electrochem 32:1287–1295
21. Fedrizzi L, Rossi S, Cristel R, Bonora PL (2004) Electrochim Acta 49:2803–2814
22. Barletta M, Bolelli G, Bonferroni B, Lusvarghi L (2010) J Thermal Spray Technol 19:358–367
23. Creus J, Idrissi H, Mazille H, Sanchette F, Jacquot P (1998) Surf Eng 14:432–436
24. Creus J, Idrissi H, Mazille H, Sanchette F, Jacquot P (1998) Surf Coat Technol 107:183–190
25. Creus J, Billard A, Sanchette F (2004) Thin Solid Films 466:1–9
26. Creus J, Mazille H, Idrissi H (2000) Surf Coat Technol 130:224–232
27. Vinayo MH, Kassabji F, Guyamont J, Fauchais P (1985) J Vac Sci Technol 3A:2483–2489
28. Li CJ, Ohmori A, Harada Y (1996) J Mater Sci 31:785–794
29. Stewart DA, Shipway PH, McCartney DG (1998) Surf Coat Technol 105:13–24
30. Sahraoui T, Guessasma S, Ali Jeridane M, Hadji M (2010) Mater Des 31:1431–1437
31. Thiele S, Kerstin S, Jaenicke-Roessler K, Berger-Lutz M, Spatzier J (2010) Thermophysical and microstructural studies on thermally sprayed Tungsten Carbide-Cobalt coatings. J Thermal Spray Technol. doi:10.1007/s11666-010-9558-0
32. Du H, Hua W, Liu J, Gong J, Sun C, Wen L (2005) Mater Sci Eng A 408:202–210
33. Creus J, Top EH, Savall C, Refait Ph, Ducros C, Sanchette F (2008) Surf Coat Technol 202:4047–4055
34. Berziou C, Remy K, Billard A, Creus J (2007) Corros Sci 49:4276–4295
35. Sanchette F, Ducros C, Billard A, Rébéré C, Berziou C, Reffass M, Creus J (2009) Thin Solid Films 518:1575–1580
36. Reffass M, Berziou C, Rébéré C, Billard A, Creus J (2010) Corros Sci 52:3615–3623
37. Kaciulis S, Mezzi A, Montesperelli G, Lamastra F, Rapone M, Casadei F, Valente T, Gusmano G (2006) Surf Coat Technol 201:313–319
38. William Grips VK, Barshilia HC, Selvi VE, Rajam Kalvati KS (2006) Thin Solid Films 514:204–211
39. Liu C, Bi Q, Leyland A, Mathews A (2003) Corros Sci 45:1243–1256
40. Brug GJ, Van Den Eeden ALG, Sluyters-Rehbach M, Sluyters JH (1984) J Electroanal Chem 176:275–295
41. Davis JR (2004) Handbook of thermal spray technology. ASM International, Ohio
42. Zhao L, Maurer M, Fischer F, Dicks R (2004) Wear 257:41–46
43. Bartuli C, Valente T, Cipri F, Bemporad E, Tului M (2005) J Thermal Spray Technol 14:187–195
44. Perez FR, Barrero CA, Arnache O, Sanchez LC, Garcia KE, Hight Walker AR (2009) Phys B Condens Matter 404:1347–1353
45. Gorockiewicz R, Lapinski A (2010) Vac 85:429–433
46. Refait Ph, Memet JB, Bon C, Sabot R, Génin JMR (2003) Corros Sci 45:833–845
47. Doncescu A, Festy D, Gil O, Maillot V, Touzain S, Tribollet B (1998) Mater Sci Forum 289–292:1163–1180
48. Dandeu A, Humbert B, Carteret C, Muhr H, Plasari E, Bossoutrot JM (2006) Chem Eng Technol 29:221–225
49. Tlili MM, Ben Amor M, Gabrielli G, Joiret S, Maurin G, Rousseau P (2001) J Raman Spectrosc 33:10–16
50. Antony H, Legrand L, Maréchal L, Perrin S, Dillmann Ph, Chaussé A (2005) Electrochim Acta 51:745–754
51. Xu X, Zhao Y, Lai Q, Hao Y (2010) J Appl Polym Sci 119:319–324
52. Sarkar A, Mahapatra S (2010) Cryst Growth Des 10:2129–2135